

A COMPARISON OF STELLAR AND GASEOUS KINEMATICS IN THE NUCLEI OF ACTIVE GALAXIES

JENNY E. GREENE

Harvard-Smithsonian Center for Astrophysics, 60 Garden St., Cambridge, MA 02138

AND

LUIS C. HO

The Observatories of the Carnegie Institution of Washington, 813 Santa Barbara St., Pasadena, CA 91101

to appear in The Astrophysical Journal.

ABSTRACT

To investigate the relationship between black holes and their host galaxies, many groups have used the width of the [O III] $\lambda 5007$ line as a substitute for the stellar velocity dispersion (σ_*) of galaxy bulges. We directly test this assumption with a large and homogeneous sample of narrow-line active galactic nuclei from the Sloan Digital Sky Survey. We consider multiple transitions ([O II] $\lambda 3727$, [O III] $\lambda 5007$, and [S II] $\lambda\lambda 6716, 6731$) and various techniques for quantifying the line width in order to obtain a calibration between the gas velocity dispersion, σ_g , and σ_* . We find that σ_g of the low-ionization lines traces σ_* , as does σ_g for the core of [O III] after its asymmetric blue wing is properly removed, although in all cases the correlation between σ_g and σ_* has considerable scatter. While the gas kinematics of the narrow-line region of active galaxies are primarily governed by the gravitational potential of the stars, the accretion rate, as traced by the Eddington luminosity ratio, seems to play an important secondary role. Departures from virial motions correlate systematically with accretion rate. We discuss the implications of these results for previous studies that use [O III] line widths to infer stellar velocity dispersions in quasars and narrow-line Seyfert 1 galaxies.

Subject headings: galaxies: active — galaxies: kinematics and dynamics — galaxies: nuclei — galaxies: Seyfert

1. INTRODUCTION

The recent discovery of a tight correlation between stellar bulge velocity dispersion and central black hole (BH) mass (the $M_{\text{BH}} - \sigma_*$ relation) strongly indicates that BHs coevolve with their host galaxies (Gebhardt et al. 2000a; Ferrarese & Merritt 2000; Tremaine et al. 2002). The growth and accretion histories of BHs appear to be inextricably linked with the mass assembly of galaxies. Thus, the evolution of BH mass density over cosmic time provides observational constraints on galaxy evolution. The $M_{\text{BH}} - \sigma_*$ relation allows us to track BH mass density with time, provided we can measure a velocity dispersion for a given system.

Unfortunately, the bulge stellar velocity dispersion is often difficult to measure directly. In active galaxies the stellar absorption features are quickly swamped by nonstellar emission from the nucleus. There is consequently a disconnect between the methods used to obtain BH masses for active galactic nuclei (AGNs) and quiescent galaxies. While locally it is possible to infer a BH mass function based on the distribution of stellar velocity dispersion (e.g., Yu & Tremaine 2002), at significant distances we must rely on AGNs, which are significantly brighter than stellar light. The challenge remains to develop secondary estimators of BH masses in AGNs and assure ourselves that AGNs follow the same $M_{\text{BH}} - \sigma_*$ relation.

Luckily, there are a number of secondary techniques in development. Reverberation mapping provides a virial estimate of BH mass to within a factor that depends on the geometry of the broad-line region (BLR) (e.g., Kaspi et al. 2000; Peterson et al. 2004). This factor can be empirically determined through comparison of M_{BH} inferred from σ_* and the reverberation mapping mass (Gebhardt et al. 2000b; Ferrarese et al. 2001; Nelson et al. 2004; Onken et al. 2004). Reverberation mapping also provides

an empirical calibration between AGN luminosity and BLR radius, which may be combined with a BLR velocity to yield a virial mass estimate (e.g., Kaspi et al. 2000). This technique has been used widely in the literature (e.g., McLure & Dunlop 2004) to study the cosmic evolution of BH mass density.

In addition to secondary mass estimates for the BH, there is a secondary technique to estimate σ_* using the velocity dispersion of the ionized gas (σ_g) from the narrow-line region (NLR). The NLR is in a privileged position in the galaxy: compact enough to be illuminated by the active nucleus and yet large enough to feel the gravitational forces of the bulge. Early studies of integrated line profiles determined that gravity, not nuclear activity, dominates the global kinematics of the NLR (Wilson & Heckman 1985; Whittle 1992a,b). Most recently, Nelson & Whittle (1996) find $\sigma_g \simeq \sigma_*$ for a sample of 66 Seyfert galaxies. These studies all measure the width of [O III] $\lambda 5007$ because it is a strong and ubiquitous line. It seems that neither rotational support nor nuclear activity is important compared to pressure support for the NLR, so that σ_g can be used as a proxy for σ_* . Of course, NLR gas velocity dispersion, particularly of the [O III] line, is easier to measure for both active and distant objects. Many subsequent studies have used the full-width at half maximum (FWHM) of [O III] as a proxy for σ_* . Nelson (2000) compares M_{BH} inferred from σ_g to reverberation-mapped masses, while Boroson (2002) compares σ_g to virial masses estimated using the line width-luminosity relation. Shields et al. (2003) compare the cosmic evolution of BH mass to the evolution of bulge velocity dispersion as inferred from σ_g , while both Grupe & Mathur (2004) and Wang & Lu (2001) investigate the BH mass distribution of narrow-line Seyfert 1 galaxies (NLS1s) using σ_g .

Despite the widespread use of σ_g , caution is in order. While, to first order, the NLR kinematics seem to be determined by

gravity, the effects of the AGN are also apparent. First of all, the [O III] line often has a broad blue wing (Heckman et al. 1981; De Robertis & Osterbrock 1984; Whittle 1985a; Wilson & Heckman 1985 and references therein) and Whittle (1992b) finds that powerful, compact linear radio sources have anomalously broad [O III] lines. At least in some cases nuclear activity directly affects the NLR kinematics, and perhaps for these systems a different emission line, one originating farther from the central source, would be a better tracer of σ_* . It is also conceivable that rotation provides a significant source of support for the gas in some fraction of NLRs, thus lowering σ_g relative to σ_* . In short, it remains to be demonstrated with a large and homogenous data set that σ_g truly traces σ_* . The data for such a study are now readily available from the Sloan Digital Sky Survey (SDSS; York et al. 2000; Stoughton et al. 2002). Using the database presented by Brinchmann et al. (2004a) we directly compare σ_g and σ_* for a large sample of narrow-line AGNs from the SDSS. In addition to the conventional [O III] line, we consider the [O II] $\lambda\lambda 3726, 3729$ and [S II] $\lambda\lambda 6716, 6731$ doublets. While these lines are problematic due to blending, and are typically weaker than the [O III] line, they are less contaminated by strong asymmetries (as we show below). In addition, the [O II] line is observable to higher redshift.

Ionized gas kinematics in the centers of galaxies is of broader interest than simply as a BH mass indicator. The structure and kinematics of the gas relative to the stars may provide clues about the dynamical history of the galaxy (e.g., Sofue & Rubin 2001). In many cases, it seems that the gas rotates more slowly than the stars, in both elliptical (e.g., Caldwell, Kirshner, & Richstone 1986; Cinzano & van der Marel 1994) and spiral galaxies (Fillmore, Boroson, & Dressler 1986; Kent 1988; Kormendy & Westpfahl 1989; Bertola et al. 1995; Fisher 1997; Cinzano et al. 1999). As noted by many of these authors, this may indicate significant pressure support for the gas. On the other hand, Vega Beltrán et al. (2001) find the gas in the centers of ~ 20 disk galaxies is moving on circular orbits in a cold disk. Presumably, a variety of dynamical states are possible for the nuclear gas. It would be interesting to examine this question with a statistical sample such as SDSS. In particular, is there anything special about the dynamical state of the ionized gas in AGNs?

We note that we are by no means the first to perform an analysis of this type. Earlier studies have looked in detail at both the [O III] line shape as an indicator of the kinematics of the NLR and at the correlation of the line width with other nuclear and host properties (for a review, see Wilson & Heckman 1985 and references therein; Nelson & Whittle 1996). The new aspect of this work is the large, homogenous sample considered. It is also, to our knowledge, the first systematic investigation of the behavior of the [S II] and [O II] line profiles. Furthermore, this is the first systematic investigation of NLR kinematics since the discovery of the $M_{\text{BH}} - \sigma_*$ relation. Not only does this provide new motivation for a better understanding of the $\sigma_g - \sigma_*$ relation, but it enables us to examine the kinematics of the NLR in relation to the physical properties of the AGN. In particular, we find that the accretion rate of material onto the BH partially determines the kinematics of the NLR.

2. THE SAMPLE

The Second Data Release (DR2) of the SDSS (Abazajian et al. 2004), with 375,000 galaxy spectra, enables us to compare nuclear gas and stellar kinematics with a large, homogeneous sample. The reader is referred to the project website for more details, as well as a complete bibliography for the survey¹. Briefly, spectroscopic candidates are selected based on imaging in the u , g , r , i , and z bands (Fukugita et al. 1996; Smith et al. 2002; Strauss et al. 2002) with a drift-scan camera (Gunn et al. 1998). Spectra are acquired with a pair of fiber-fed spectrographs. Each fiber subtends a diameter of 3'', corresponding to ~ 5.4 kpc at $z = 0.1$. The spectra have an instrumental resolution of $\lambda/\Delta\lambda \approx 1800$ ($\sigma_{\text{inst}} \approx 71$ km s $^{-1}$). Integration times are determined for a minimum signal-to-noise ratio (S/N) of 4 at $g = 20.2$ mag. The spectroscopic pipeline performs basic image calibrations, as well as spectral extraction, sky subtraction, removal of atmospheric absorption bands, and wavelength and spectrophotometric calibration (Stoughton et al. 2002).

Recently, the SDSS team at MPA/JHU made publicly available their database of galaxy properties for 211,894 galaxies, including 33,589 narrow-line (Type 2) AGNs from DR2². The sample selection and spectral treatment are discussed in detail in Kauffmann et al. (2003a). Like the main galaxy sample, the redshift distribution is strongly peaked at $z \approx 0.1$, and H α is always present in the band. AGNs are selected based on their location in line intensity ratio diagnostic diagrams (Baldwin, Phillips, & Terlevich 1981; Veilleux & Osterbrock 1987; Kauffmann et al. 2003c) after the stellar continuum is modeled and removed using stellar population synthesis models. Their definition of AGNs is very inclusive. Only objects solidly on the stellar locus are excluded, while low-ionization nuclear emission-line regions (LINERs; Heckman 1980) and transition objects (Ho, Filippenko, & Sargent 1993) are included. The database includes the line intensities used to make the selection. They also make available stellar velocity dispersions, measured using a direct-fitting algorithm that assumes Gaussian velocity profiles (Heckman et al. 2004).

We selected our sample from this set of narrow-line AGNs. Using the tabulated emission-line ratios, we use the line-ratio diagnostics outlined in Ho, Filippenko, & Sargent (1997a) to explicitly include only Type 2 Seyferts, excluding both LINERs and transition objects. This guarantees that the emission lines are dominated by AGN light. As discussed in Ho (2004), the large physical scales subtended by the SDSS fibers very likely includes substantial host galaxy emission, which presents a source of confusion for interpreting LINERs and transition objects. We further require [O II], [O III], and [S II] to have a S/N per pixel greater than at least 3 in the line, and a measured stellar velocity dispersion. The mean equivalent widths (EWs) for the resulting sample are 18 for [O II], 20 for [O III], and 4 for [S II], the weakest line. In §3.4 we limit our sample to objects having only the highest-EW lines to examine how the S/N affects our results. We exclude all objects with σ_* below the nominal SDSS instrumental resolution of $\sigma_{\text{inst}} \approx 70$ km s $^{-1}$ (as in Heckman et al. 2004). We further exclude a handful of objects with $\sigma_* > 400$ km s $^{-1}$ as most likely unphysical (10 objects had $\sigma_* \approx 600$ km s $^{-1}$)³ and 13 objects for which one of the line detections appeared marginal after manual inspection. This left a sample of 2050 objects. As described below, we also remove objects with double-peaked or unresolved line profiles,

¹<http://www.sdss.org/>

²<http://www.mpa-garching.mpg.de/SDSS/>

³The distribution function of velocity dispersions for local early-type galaxies drops sharply for $\sigma_* > 400$ km s $^{-1}$ (Sheth et al. 2003).

leaving a final sample of 1749 objects. The median redshift of the sample is $z \approx 0.1$, the same as the SDSS in general.

Throughout we assume the following cosmological parameters to derive distances: $H_0 = 100h = 72 \text{ km s}^{-1} \text{ Mpc}^{-1}$, $\Omega_m = 0.3$, and $\Omega_\Lambda = 0.7$.

3. DATA ANALYSIS

We wish to compare the stellar and gas line widths for the entire AGN sample. Since the stellar velocity dispersions have been measured, we need only remove the stellar continuum and then measure the gas line widths. Below we describe each of those steps.

3.1. Continuum Subtraction

In order to measure reliable line widths, the underlying stellar continuum must be removed. Continuum variations can hide or mimic broad line wings and skew relative line intensity measurements. Since the MPA/JHU database does not provide continuum-subtracted spectra, we have to repeat this step of the analysis. Fortunately, the SDSS survey provides a large and homogeneous library of pure absorption-line galaxies for use in continuum subtraction. We use a code that employs principal component analysis, kindly provided by Lei Hao (Hao et al. 2005). A library of hundreds of spectra is projected onto an orthogonal basis of eigenspectra. Typically eight eigen-components are sufficient to provide an adequate model of the stellar spectrum. A power-law continuum and an A star spectrum may be included if necessary.

3.2. Profile Fitting

There are many possible ways to parameterize emission-line profiles. Some of the most common include the FWHM and the second moment of the line, defined to be

$$\sigma^2 = (c/\lambda_c)^2 \int (\lambda - \lambda_c)^2 f_\lambda d\lambda / \int f_\lambda d\lambda.$$

The line centroid is λ_c , f_λ is the flux density in the continuum-subtracted spectrum, and σ is in units of km s^{-1} . For a pure Gaussian the second moment is equal to σ and $\text{FWHM} = \sigma/2.35$. (The second moment is directly comparable to the stellar velocity dispersion measurements, which assume a Gaussian broadening function.) If to this original Gaussian we added a broad, low-contrast Gaussian to represent the line wings, the FWHM would increase slightly, by an amount depending on the contrast between the core and the wings. The second moment, on the other hand, is more sensitive to the presence of wings, and becomes significantly broader. For this reason, we get more information on the full line profile from the second moment. Unfortunately, measurements of the second moment can be very sensitive to the S/N of the spectrum. Therefore, we first fit a multi-component Gaussian to the line profile, and then measure the second moment from the model profile, as described below. This technique has the further benefit of providing a decomposition of the core and wing components, so that we can examine the distribution of core and wing widths independently.

After much experimentation, we find that the most reliable method, applicable to the majority of objects, is to fit each

profile with two Gaussians, one representing the line core and the other representing the line wing. The second component is fixed initially to be blueward of the central component, although in a subset of cases ($\sim 6\%$), a redshifted component was required for an acceptable fit. If the fit with a second component improves significantly (at least 20% increase in χ^2) over the single-component fit, it is kept. We use this model to simultaneously fit the $[\text{O III}] \lambda\lambda 4959, 5007$ lines, with their separation fixed and their relative strength constrained to the theoretical ratio of 3:1. Likewise, the $[\text{S II}] \lambda\lambda 6716, 6731$ lines are fixed to the same profile⁴, with their separation fixed to the laboratory value; the ratio of the line intensities varies with density, and is allowed to vary in the fit. The $[\text{O II}] \lambda\lambda 3726, 3729$ lines behave similarly, but the decomposition is more difficult because the expected line widths are comparable to the pair separation (2.8 \AA or 225 km s^{-1}). For this reason, we allow the line ratio to vary between 0.2 and 1.4, the expected range for the typical densities observed in the NLR (e.g., Osterbrock 1989). Sample fits are shown in Figure 1.

As in previous studies, the majority of the line profiles are smooth, but a small percentage are lumpy, and some have two distinct peaks with comparable flux and line width. We find 31 of the 2050 ($\sim 1\%$) objects with clearly defined double peaks (Fig. 1). While we show below that in general the NLR is not rotationally dominated, we suspect that in these cases the NLR gas is predominantly organized into a disk. Of course, bipolar outflows may also be responsible for the double-peaked lines. In any case, these objects are such clear outliers that we exclude them from further consideration.

3.3. Instrumental Resolution

The observed σ is the convolution of the true line width and the instrumental response. To first order, the intrinsic line width can be approximated by $\sigma = \sqrt{\sigma_{\text{obs}}^2 - \sigma_{\text{inst}}^2}$. In the case of the SDSS data, σ_{inst} varies not only as a function of wavelength, but also the location of the object on the plate and the temperature on the night of the observations. For this reason, the SDSS pipeline measures the instrumental response using an arc lamp spectrum, and returns the resolution at every pixel. The mean values for this sample are $74 \pm 8 \text{ km s}^{-1}$ for $[\text{O II}]$, $60 \pm 5 \text{ km s}^{-1}$ for $[\text{O III}]$, and $56 \pm 5 \text{ km s}^{-1}$ for $[\text{S II}]$. When we remove the effects of instrumental resolution, some of the objects become unresolved. Measurements below the resolution limit are not reliable, and so we remove all objects for which one or more of the lines in question is unresolved, leaving a total of 1749 objects.

3.4. Errors and Uncertainties

The average formal error in σ_g is $\sim 5\%$. However, this estimate neglects systematic effects, the two most serious of which are uncertainties in the continuum subtraction and component decomposition. The latter is only a concern in the case of $[\text{O III}]$, the only line that often requires a two-component fit. In some cases, there is ambiguity as to the exact decomposition between these two. However, we do not believe errors in decomposition introduce any systematic bias. There are publicly available error estimates⁵ for the stellar velocity dispersions we

⁴If the NLR is stratified in density, the width of each component of the doublet can be different, since their critical densities are different. But the profile differences are expected to be small and hard to discern with data of moderate S/N.

⁵<http://spectro.princeton.edu/>

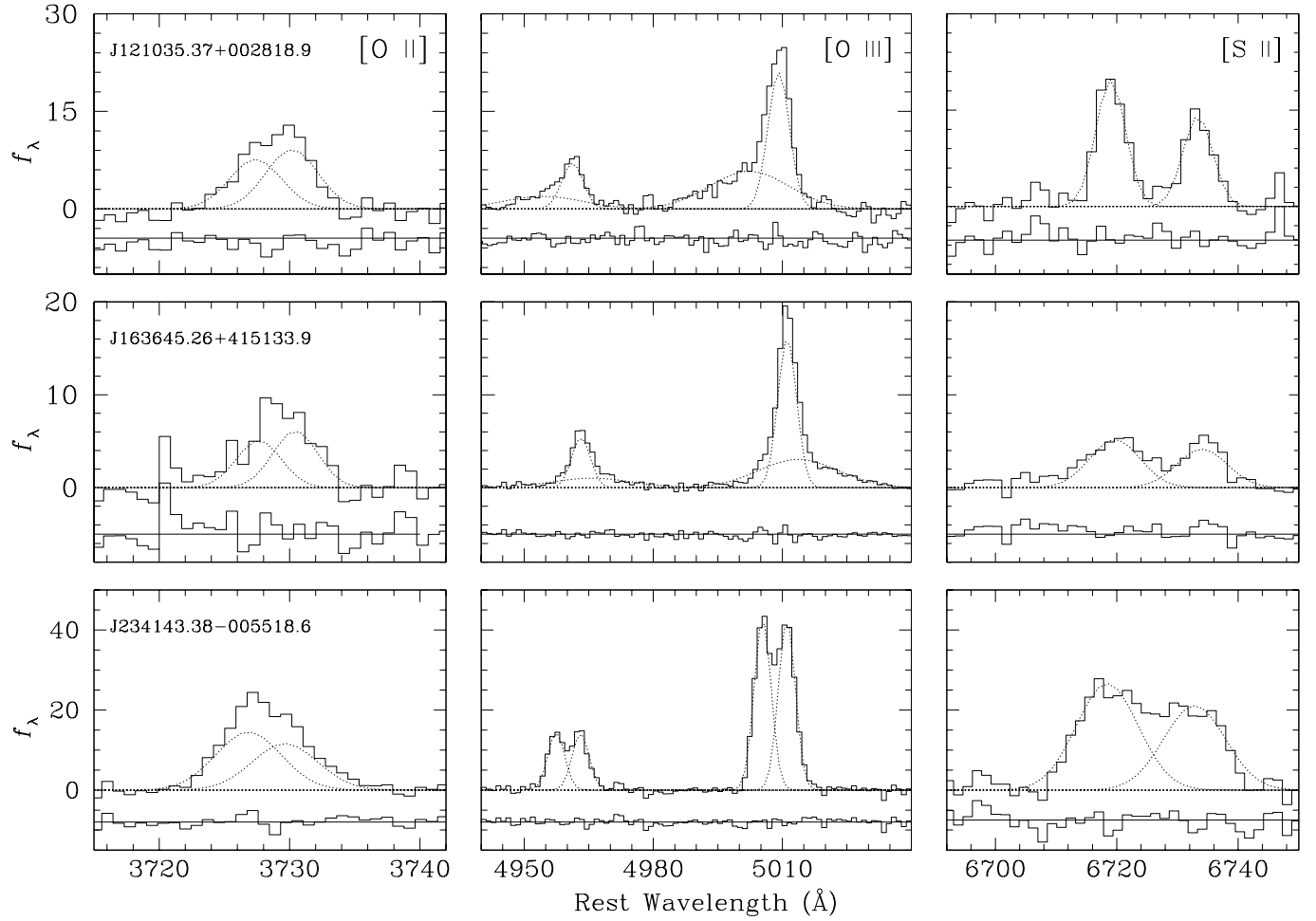


FIG. 1.— Sample fits for blue-asymmetric (top), red-asymmetric (middle), and double-peaked (bottom) objects. The ordinate of the plots are in units of 10^{-17} erg $s^{-1} cm^{-2} \text{Å}^{-1}$. The ordinate scales are 1:1:0.33 (top), 1:3:1 (middle), and 1:1:0.2 (bottom). Note the hint of double-peakedness in the [S II] profile (bottom).

Table 1. Statistical Results

Sample (1)	Number (2)	$\langle \sigma_{[\text{OII}]} / \sigma_* \rangle$ (3)	$\langle \sigma_{[\text{SII}]} / \sigma_* \rangle$ (4)	$\langle \sigma_{[\text{OIII}]} / \sigma_* \rangle$ (5)	$\langle \sigma_{[\text{OIII}]}^c / \sigma_* \rangle$ (6)
All	1749	1.13 ± 0.38	1.11 ± 0.35	1.34 ± 0.66	1.00 ± 0.35
High EW	657	1.19 ± 0.45	1.15 ± 0.38	1.40 ± 0.53	0.98 ± 0.35
Low z	736	1.17 ± 0.39	1.16 ± 0.37	1.43 ± 0.75	1.01 ± 0.35
Moderate z	957	1.11 ± 0.37	1.09 ± 0.34	1.28 ± 0.57	1.00 ± 0.35
High z	957	0.99 ± 0.35	1.00 ± 0.36	1.19 ± 0.53	0.95 ± 0.27
Low $H\alpha$	872	1.13 ± 0.38	1.13 ± 0.38	1.28 ± 0.67	1.04 ± 0.35
High $H\alpha$	877	1.14 ± 0.38	1.10 ± 0.32	1.40 ± 0.63	0.97 ± 0.34
No radio	1475	1.12 ± 0.37	1.10 ± 0.34	1.29 ± 0.59	1.00 ± 0.34
Low radio	119	1.27 ± 0.43	1.34 ± 0.47	1.80 ± 0.99	1.06 ± 0.41
High radio	133	1.20 ± 0.43	1.12 ± 0.34	1.56 ± 0.76	1.01 ± 0.41
Lobes	23	0.99 ± 0.40	0.93 ± 0.32	1.00 ± 0.44	0.75 ± 0.22

Note. — *Samples* High EW: EW([OII])> 25 Å, EW([OIII]) > 20 Å, and EW([SII]) > 5 Å, data from Brinchmann et al. 2004a. Low z : $z < 0.1$. Moderate z : $0.1 < z < 0.2$. High z : $z > 0.2$. Low $H\alpha$: $L_{H\alpha} < 10^{40.7}$ erg s $^{-1}$. High $H\alpha$: $L_{H\alpha} > 10^{40.7}$ erg s $^{-1}$. No radio: no detection in FIRST. Low radio: $P_{20\text{cm}} < 10^{22.5}$ W Hz $^{-1}$. High radio: $P_{20\text{cm}} > 10^{22.5}$ W Hz $^{-1}$. Lobes: Spatially extended in FIRST.

are using. The median error is $\sim 8\%$, or ~ 12 km s $^{-1}$ at the median $\sigma_* \approx 144$ km s $^{-1}$. These uncertainties are small compared to the scatter in $\langle \sigma_g / \sigma_* \rangle$, the quantity central to our analysis in this paper.

We can investigate the extent to which the scatter is due to measurement error by limiting the sample to a subset of high-EW objects for which the formal measurement errors are small. We limit the sample to the strongest ~ 500 objects for each line. We find no significant difference in either the mean value or the scatter around σ_g (see entries in Table 1). This suggests that the scatter is dominated by intrinsic variations, rather than measurement errors. In the Appendix we specifically examine the scatter introduced by rotational broadening. We find that it is also insufficient to account for the observed scatter.

4. RESULTS

4.1. Primary Driver: Gravitational Potential of the Bulge

Our findings are summarized in Table 1, which shows $\langle \sigma_g / \sigma_* \rangle$ for each transition. Our primary result is that the line widths of [S II] and [O II] track the stellar velocity dispersion in the mean, albeit with substantial scatter. The width of [O III], on the other hand, is on average significantly broader than σ_* ; $\sigma_{[\text{OIII}]}$ cannot be used directly as a tracer of σ_* . However, as we discuss below, the core of [O III] does track σ_* .

The different behavior of the low-ionization lines compared to [O III] can be understood in terms of well-known variations in line shape as a function of critical density and ionization potential within the NLR (e.g., Pelat, Alloin, & Fosbury 1981; Filippenko & Halpern 1984; Filippenko 1985; De Robertis & Osterbrock 1986). The NLR is stratified in density such that lines of higher critical density originate from closer to the nucleus. Since the critical density of [O III] $\lambda 5007$ is higher than those of [O II] $\lambda 3727$ and [S II] $\lambda\lambda 6716, 6731$ (Osterbrock 1989), in a density-stratified NLR we expect [O III] to be broader

than [O II] and [S II], whereas [O II] and [S II] should share similar line widths. As expected, we find that $\langle \sigma_{[\text{OIII}]} / \sigma_{[\text{OII}]} \rangle$ and $\langle \sigma_{[\text{OIII}]} / \sigma_{[\text{SII}]} \rangle \approx 1.2 \pm 0.5$, while $\langle \sigma_{[\text{SII}]} / \sigma_{[\text{OII}]} \rangle \approx 1.0 \pm 0.3$. This suggests that the [O III] emission originates from closer to the nucleus than the other lines.

As noted, our results suggest that the kinematics of low-ionization gas in the NLR is dominated by gravity, such that the velocity dispersion in the gas and stars are comparable. On the other hand, the [O III] line width is significantly broader than σ_* , suggesting that the active nucleus plays a significant role in governing the kinematics of the [O III]-emitting gas. Taken at face value, this finding seems to contradict the conclusions of Nelson & Whittle (1996), who have argued that the [O III] line width is largely dominated by gravity. Since the [O III] profile is invariably asymmetric, characterized by a central core component plus a high-velocity blue wing, it is reasonable to suppose that the line core should have the closest affinity to any gravitationally dominated component. Using our two-component Gaussian fits to the [O III] profiles, we can directly compare the core velocity dispersion with σ_* . The result of this test is shown in the last column of Table 1. Indeed, we find that when the blue wing is removed, the core of the [O III] line statistically traces σ_* , again with significant scatter. This suggests that the low-velocity gas in the line core is gravitationally dominated, while the wing is more strongly influenced by the active nucleus.

4.2. Secondary Drivers

We now look for secondary parameters to explain the deviations of σ_g for the [O III] line compared to σ_* , which are plausibly related to either the active nucleus or the environment. Looking at the correlation of these deviations with various indicators of nuclear activity may reveal useful information about the interaction of the nucleus with the NLR. We consider host galaxy morphology, local environment, star forma-

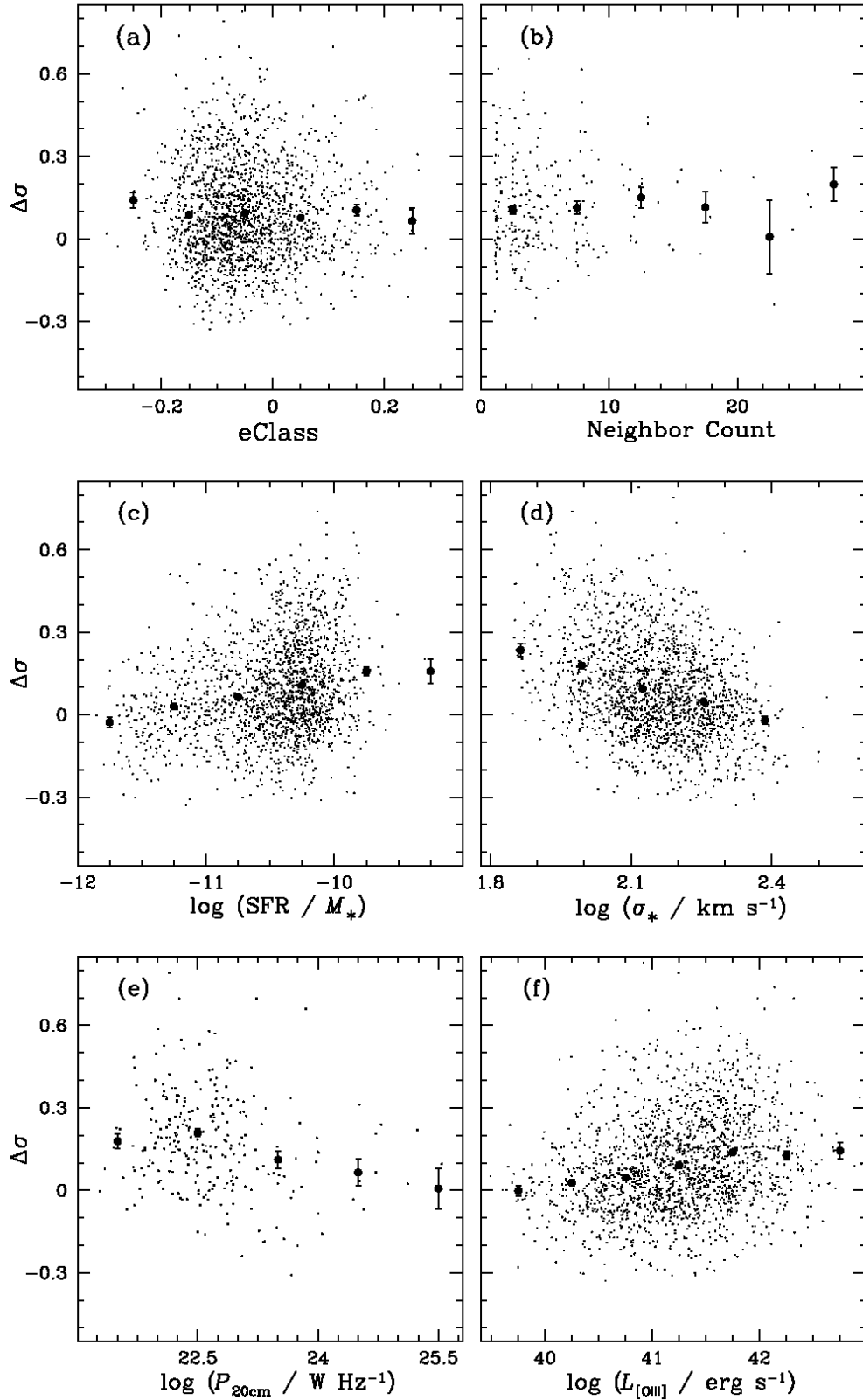


FIG. 2.— Deviations from virial line width, $\Delta\sigma \equiv \log \sigma_{\text{[OIII]}} - \log \sigma_*$, with various parameters: (a) eClass, (b) neighbor count, (c) median total star formation rate normalized to the galaxy stellar mass (yr^{-1}), (d) σ_* , (e) radio power, and (f) [O III] luminosity. In all cases, filled circles show the mean value plotted in the middle of the bin, and error bars are the standard deviation in the mean.

tion rate, and bulge stellar velocity dispersion as global variables. In terms of nuclear effects, we look at radio power, AGN luminosity, and Eddington ratio [$L_{\text{bol}}/L_{\text{Edd}}$, where $L_{\text{Edd}} \equiv 1.26 \times 10^{38} \text{ erg s}^{-1} (M_{\text{BH}}/M_{\odot})$]. In particular, we will examine the correlation of each of the above properties with $\Delta\sigma \equiv \log \sigma_{[\text{OIII}]} - \log \sigma_*$. In Figure 2 we show $\Delta\sigma$ plotted against each variable, with binned values overplotted to highlight any underlying trend. The large, binned points represent the mean and standard deviation in the mean plotted at the bin center.

Of additional interest is whether the characteristics of the blue wing correlate with any of the properties listed above. In order to investigate this question we looked at three wing diagnostics: the width of the blue wing, the flux ratio between the core and the wing, and the wavelength shift between the core and the wing. We found no strong correlations between any of the above quantities with either the nuclear or global variables.

4.2.1. Global Properties

Both gas and stellar kinematics in the central regions of galaxies may depend on Hubble type. We cannot derive robust morphologies directly from the SDSS data because the resolution and depth are insufficient. However, Shimasaku et al. (2001) and Strateva et al. (2001) find that the color, concentration index, and spectral decomposition provided by the SDSS pipeline all correlate well with standard morphological classifications. We use two different integrated properties to estimate the morphological distribution of the sample. The “eClass” is a spectroscopic classification derived from the principal component analysis decomposition of each galaxy spectrum, and ranges from -0.35 for early-type galaxies to $+0.5$ for late-type galaxies. The “concentration index,” the ratio of the radii enclosing 90% and 50% of the light in the r band, describes the compactness of the stellar emission. Concentrations indices larger than 2.6 correspond to early-type galaxies. The mean concentration index of 2.65 and mean eClass of -0.05 are both consistent with a population of early-type galaxies (Kauffmann et al. 2003c). We see no trend with $\Delta\sigma$ in either of these parameters (see Fig. 2a for $\Delta\sigma$ vs. eClass).

Nelson & Whittle (1996) find evidence for broadened line widths in noticeably disturbed systems. While we cannot use the SDSS imaging to reliably gauge disturbance levels, we can look for systematic trends with local galaxy density. Kauffmann et al. (2004) find an increase of nuclear activity and star formation for AGNs in overdense regions. We might, therefore, expect some correlation between environmental density and line width. However, we find no evidence for a trend. The luminosity-weighted neighbor counts are plotted against $\Delta\sigma$ for those objects with measured neighbor counts in Figure 2b.

Depending on the origin of the ionized gas, star formation (particularly in the nuclear regions) could affect the gas kinematics. Recent studies, such as that of Kauffmann et al. (2004), suggest a link between star formation and nuclear activity. If this is the case, then stellar winds from massive stars or supernova feedback may impact the dynamical state of the nuclear gas. To investigate this possibility, we use the total star formation rate per unit stellar mass (SFR/M_*) from Brinchmann et al. (2004b), which is derived for the AGN sample using a relation between the 4000 \AA -break and SFR in a sample of star-forming galaxies. In Figure 2c we plot $\log \text{SFR}/M_*$ against $\Delta\sigma$; there is

no significant trend apparent.

By far the strongest trend is between $\Delta\sigma$ and σ_* (Fig. 2d), with a Spearman rank correlation coefficient of $\rho = -0.32$, and a probability of $P_{\text{null}} < 10^{-4}$ for the null hypothesis of no correlation. Massive galaxies with large values of σ_* on average have $\Delta\sigma \approx 0$, whereas less massive galaxies with smaller values of σ_* systematically have $\Delta\sigma > 0$. This trend with σ_* directly translates into a trend with BH mass, via the $M_{\text{BH}} - \sigma_*$ relation.

4.2.2. Radio Power

Many lines of evidence suggest that radio jets influence the physical and dynamical state of the NLR. Wilson & Willis (1980) found a correlation between [O III] line width and radio power. There is also a well-known relation between [O III] luminosity and radio power (de Bruyn & Wilson 1978; Ho & Peng 2001). Whittle (1985b, 1992a,b) finds evidence that strong ($L_{1415 \text{ MHz}} \gtrsim 10^{22.5} \text{ W Hz}^{-1}$), “linear”⁶ radio sources have systematically broader [O III] lines. The same effect is seen by Nelson & Whittle (1996), but the trend is weaker. It seems that the jet plasma interacts with and accelerates the NLR, thus boosting the line width. We stress that this finding holds only for compact linear radio sources. In contrast, Smith, Heckman, & Illingworth (1990) do not find supervirial [O III] line widths among powerful radio galaxies with kpc-scale jets.

In light of the above results, we extracted radio fluxes from the Faint Images of the Radio Sky at Twenty-cm (FIRST; Becker, White, & Helfand 1995) survey, which is largely coincident with the SDSS footprint. FIRST is a 20 cm survey with a sensitivity of $\sim 1 \text{ mJy}$ and a resolution $\sim 5''$. All but 279 of the sources in our sample have FIRST measurements. The SDSS pipeline only considers matches within $2''$ in order to minimize confusion (Ivezić et al. 2002). However, a small fraction of the sources will have extended sources associated with them as well. We therefore search the FIRST database with a $60''$ radius for extended sources, and find 25. The radio luminosities are K-corrected to 20 cm assuming $F_{\nu} \propto \nu^{-0.46}$, which is the median spectral slope found by Ho & Ulvestad (2001) for nearby Seyfert galaxies. Unfortunately, while the FIRST database is homogeneous and complete, the resolution is not sufficient to resolve nuclear morphology. Nevertheless, for completeness we consider possible trends with $\Delta\sigma$.

Our results are ambiguous (see Fig. 2e). As can be seen from Table 1, the presence of core radio emission seems to have no impact on the observed line widths. On the other hand, extended radio sources appear to have marginally *narrower* line widths. We attribute the ambiguous results to the low sensitivity and resolution in the radio data. The correlation previously discovered holds for linear radio cores only. With $5''$ resolution, we cannot discriminate between different core morphologies. Furthermore, the sensitivity limit of $\sim 1 \text{ mJy}$ corresponds to $P_{20\text{cm}} = 2.5 \times 10^{22} \text{ W Hz}^{-1}$, at the “powerful” limit considered by Whittle (1992b).

4.2.3. AGN Luminosity and Eddington Ratio

Perhaps the most basic question to ask is whether the energy output of the active nucleus is directly related to $\Delta\sigma$. We use emission-line ($\text{H}\alpha$ and [O III]) luminosity as a surrogate for the AGN luminosity (Adams & Weedman 1975; Yee & Oke 1978; Yee 1980). We derive $L_{\text{H}\alpha}$ and $L_{[\text{OIII}]}$ from the fluxes given in

⁶The “linear” classification for the above studies comes from the high-resolution ($0''.2$ – $0''.6$ or 80 – 400 pc) study of Ulvestad & Wilson (1984). Linear sources have extended radio emission on sub-galactic scales (tens to hundreds of parsecs), as opposed to sources classified as “diffuse”, “slightly resolved”, or “unresolved.” The linear morphology suggests the presence of compact jets, not to be confused with the extended jets and radio lobes found in radio galaxies.

the database of Brinchmann et al. (2004a), corrected for Galactic extinction using the dust maps of Schlegel, Finkbeiner, & Davis (1998). We find no evidence for a strong trend with either quantity (see Fig. 2f for $L_{\text{[OIII]}}$), at least for the relatively limited range of luminosities probed here. This result does not change for a high-EW subsample.

In addition to the luminosity of the AGN, we can ask whether the Eddington ratio affects the NLR kinematics. The Eddington ratio, proportional to the accretion rate per unit (BH) mass, characterizes the extent to which radiation pressure competes with gravity in the nucleus. Therefore, we might expect objects with higher Eddington ratios to show larger nonvirial motions.

We do not have direct measurements of Eddington ratios for our sample, but we can estimate them by using line luminosities as a substitute for L_{bol} and σ_* as a surrogate for BH mass (and hence L_{Edd}). We stress, however, that the estimated values of $L_{\text{bol}}/L_{\text{Edd}}$ are highly uncertain. The conversion from the observed luminosity in a specific band (e.g., optical) to bolometric luminosity introduces the largest uncertainty. For Type 2 objects, the problem is compounded by the fact that the nonstellar (AGN) continuum is not directly observable in the optical. Instead, we will make use of the extinction-corrected [O III] luminosity to estimate L_{bol} , using the bolometric correction for [O III] luminosity from Heckman et al. (2004). This is derived in two steps. First, the [O III] luminosity is correlated with optical AGN continuum luminosity for a sample of Type 1 objects in SDSS (Kauffmann et al. 2003c; Zakamska et al. 2003). Then a standard bolometric correction from optical continuum to bolometric luminosity (from Marconi et al. 2004) is employed. The final derived relation becomes $L_{\text{bol}} \approx 3500 L_{\text{[OIII]}}$, with an uncertainty of 0.4 dex. We note that this estimate agrees well with the [O III] bolometric correction derived by L. C. Ho (2005, in preparation), established in a completely independent way using broad-band spectral energy distributions. The BH mass is calculated using the measured σ_* and the $M_{\text{BH}} - \sigma_*$ relation of Tremaine et al. (2002), which formally has a scatter of less than 0.21 dex.

Notwithstanding the large uncertainty in bolometric correction, we find a highly significant correlation between $\Delta\sigma$ and $L_{\text{bol}}/L_{\text{Edd}}$ (Fig. 3a). *The [O III] line width is most supervirial in objects at the highest Eddington ratio.* Formally, the Spearman rank correlation coefficient is $\rho = 0.46$, with a probability of $P_{\text{null}} < 10^{-4}$ for rejecting the null hypothesis of no correlation. For the purpose of comparing with previous work, we also calculate $\Delta\sigma$ using FWHM/2.35 rather than σ_g . Although we have argued that the FWHM is an inferior measure of line width, there are occasions in which only FWHM measurements are available in the literature. The result is shown in Figure 3b. While the slope is shallower, the trend persists ($\rho = 0.36$, $P_{\text{null}} < 10^{-4}$).

We have seen that $\Delta\sigma$ is also significantly correlated with σ_* , or, equivalently, BH mass (§4.2.1). Since $L_{\text{bol}}/L_{\text{Edd}}$ depends on BH mass, we must consider whether BH mass or $L_{\text{bol}}/L_{\text{Edd}}$ is really the fundamental parameter driving $\Delta\sigma$. Because the correlation of $\Delta\sigma$ with $L_{\text{bol}}/L_{\text{Edd}}$ ($\rho = 0.46$) is stronger than that with BH mass ($\rho = -0.32$), $L_{\text{bol}}/L_{\text{Edd}}$ appears to influence $\Delta\sigma$ more strongly than BH mass. In principle, the strongest correlation could come from some combination of the BH mass and $L_{\text{bol}}/L_{\text{Edd}}$. However, we find that including the BH mass in a partial correlation analysis (Akritas & Siebert 1996) does not improve the correlation. We therefore conclude that $L_{\text{bol}}/L_{\text{Edd}}$ is the primary physical parameter driving $\Delta\sigma$.

The solid line in Figure 3a represents our fit to the data. Using an ordinary least-squares regression with $\log L_{\text{bol}}/L_{\text{Edd}}$ as the independent variable, we find

$$\Delta\sigma = (0.131 \pm 0.006) \log L_{\text{bol}}/L_{\text{Edd}} + (0.202 \pm 0.006). \quad (1)$$

To better highlight the trend, we also binned the data in bins of $\Delta(\log L_{\text{bol}}/L_{\text{Edd}}) = 0.5$ dex, which yields the following fit (dashed line):

$$\Delta\sigma = (0.113 \pm 0.005) \log L_{\text{bol}}/L_{\text{Edd}} + (0.192 \pm 0.008). \quad (2)$$

If we calculate $\Delta\sigma$ using $\sigma_g = \text{FWHM}/2.35$ (Fig. 3b), then the corresponding relations for the unbinned and binned data are, respectively,

$$\Delta\sigma = (0.072 \pm 0.005) \log L_{\text{bol}}/L_{\text{Edd}} + (0.080 \pm 0.005) \quad (3)$$

and

$$\Delta\sigma = (0.065 \pm 0.002) \log L_{\text{bol}}/L_{\text{Edd}} + (0.077 \pm 0.004). \quad (4)$$

It is interesting to examine $\Delta\sigma$ at the extreme Eddington ratios. For objects at the lowest Eddington ratios ($\log L_{\text{bol}}/L_{\text{Edd}} \lesssim -2$ for our sample) we find line widths that are *subvirial* ($\Delta\sigma < 0$). This finding suggests that quiescent (inactive) early-type galaxies (most closely approximated by the lowest-Eddington ratio systems) have subvirial gas velocities. In support of this finding, Vega Beltrán et al. (2001) find the $\sigma_g < \sigma_*$ in early-type spirals, where the gas is at least partially rotationally supported (in contrast with late-type spirals, where both gas and stars are rotationally supported). In light of this issue, it is interesting to note that the lobe-dominated radio sources, which have been suggested to be preferentially low-Eddington ratio objects (e.g., Rees et al. 1982), also appear to have subvirial gas velocities (§ 4.2.2). We do not find a significantly low distribution of Eddington ratios among the extended radio sources in our sample, but the statistics are poor. It would be interesting to extend our study to a larger sample of extended radio sources.

At the other extreme, for $\log L_{\text{bol}}/L_{\text{Edd}} \gtrsim 1$, our results imply that σ_g systematically overestimates σ_* by $\sim 0.2 - 0.3$ dex. This strongly suggests that studies that use σ_g as a proxy for σ_* , such as that by Shields et al. (2003) or Grupe & Mathur (2004), may systematically overestimate σ_* . In both cases we expect the objects to be preferentially accreting at a high rate. Shields et al. (2003) concentrated on high-luminosity sources (QSOs) at high redshift, which would tend to be biased toward higher Eddington ratios. The study of Grupe & Mathur (2004) is concerned with NLS1s, which are thought to be preferentially high-Eddington ratio objects (e.g., Pounds, Done, & Osborne 1995). Grupe & Mathur (2004; see also Mathur, Kuraszkiewicz, & Czerny 2001), using $\text{FWHM}_{\text{[OIII]}}$ as a surrogate for σ_* , claim that NLS1s have BHs that are undermassive relative to their bulge masses. Most or all of the trend discussed by these authors may be attributed to the systematic broadening of [O III] at the highest Eddington ratios.

In Figure 4 we show a modified version of Figure 1 from Grupe & Mathur (2004). We have reproduced the figure exactly in open symbols, and then overplotted the same data with the [O III] widths corrected using our derived calibration (Eq. 3) in filled symbols. Again, while we do not advocate the use of FWHM, in this case it is the only available measure of line width. The squares are “normal” broad-line Seyfert 1s, while the circles are NLS1s, selected using the Grupe &

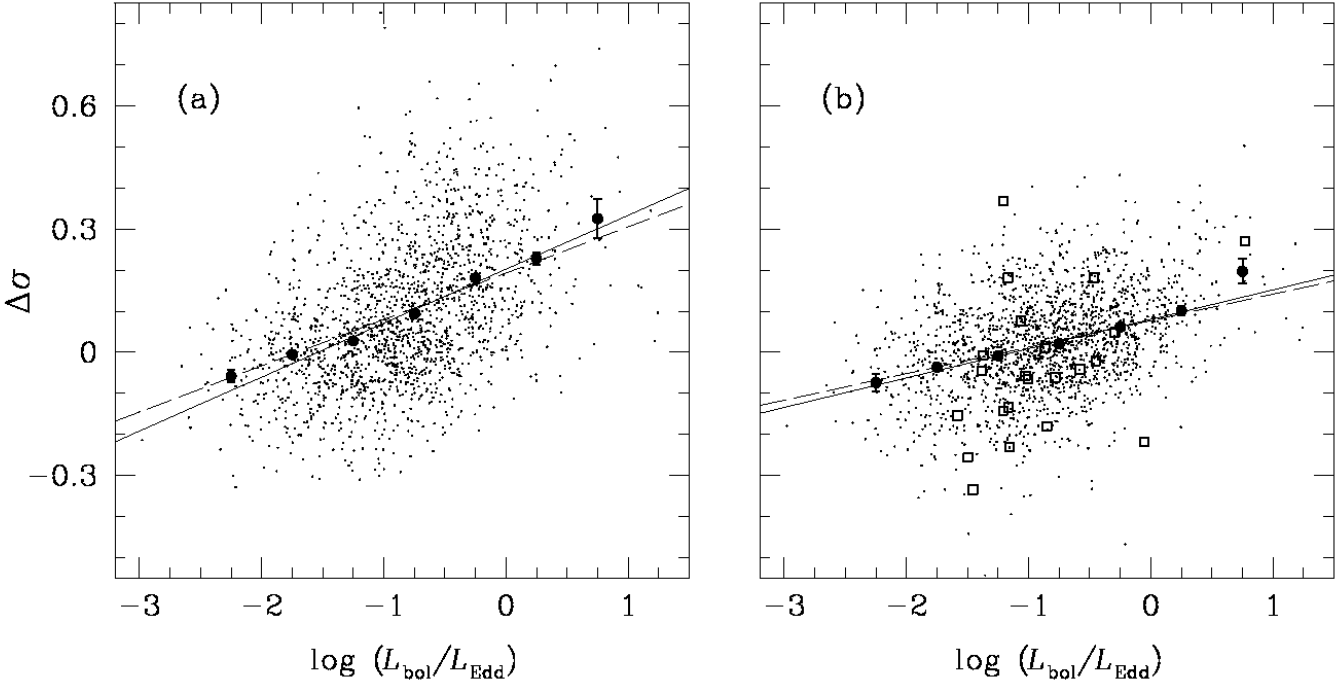


FIG. 3.— (a) $\Delta\sigma \equiv \log\sigma_{[\text{OIII}]} - \log\sigma_*$ plotted against the Eddington ratio, $L_{\text{bol}}/L_{\text{Edd}}$. Bolometric luminosity is estimated using the bolometric correction from Heckman et al. (2004); see text. Points are the SDSS sample. Large points are the mean values plotted in the center of the bin, and error bars are the standard deviation in the mean. Solid line shows the fit to data in Equation 1; dashed line shows the fit to the binned data in Equation 2. (b) Same as (a), but using $\sigma_g = \text{FWHM}/2.35$. Boxes are the Type 1 objects from the Nelson & Whittle (1996) sample. The solid and dashed lines represent Equations 3 and 4, respectively.

Mathur (2004) criterion of $\text{FWHM}(\text{H}\beta) \leq 2000 \text{ km s}^{-1}$. The M_{BH} values are derived from $\text{FWHM}(\text{H}\beta)$ and L_{5100} as tabulated in Grupe et al. (2004; corrected to our cosmology), using the line width-luminosity-mass scaling of Kaspi et al. (2000). The overplotted line represents the Tremaine et al. (2002) parameterization of the $M_{\text{BH}} - \sigma_*$ relation. The $L_{\text{bol}}/L_{\text{Edd}}$ values used for the correction are derived using the L_{bol} values provided in Grupe et al. (2004), estimated from their optical and soft X-ray data. The mean Eddington ratio for the broad-line Seyfert 1s in this sample is $\log L_{\text{bol}}/L_{\text{Edd}} = -0.74$, while for the NLS1s it is $\log L_{\text{bol}}/L_{\text{Edd}} = 0.23$, in support of the idea that NLS1s tend to be high-Eddington ratio objects. This translates into $\langle \Delta\sigma \rangle = 0.03$ for the broad-line objects, as compared to $\langle \Delta\sigma \rangle = 0.1$ for the NLS1s. As shown in Figure 4, the argument that the NLS1s lie systematically below the $M_{\text{BH}} - \sigma_*$ relation is significantly weakened. To test this statistically, we compute the perpendicular distance (d_{\perp})⁷ of each point from the Tremaine et al. (2002) line. After our correction, the two populations are no longer statistically different in d_{\perp} according to a Kolmogorov-Smirnov (K-S) test ($P_{\text{KS}} = 25\%$). In other words, the case that the BHs of NLS1s are undermassive with respect to their bulges is no longer statistically supported.

We are wary to overinterpret Figure 4, since it is based on our statistical correction for $\Delta\sigma$ and on a bolometric correction, both of which inherently have a large scatter. In actuality, the best way to establish the location of NLS1s relative to the $M_{\text{BH}} - \sigma_*$ relation is to obtain direct measurements of σ_* for them. Barth, Greene, & Ho (2005), in a systematic investiga-

tion of σ_* for the NLS1s selected from the sample of Greene & Ho (2004), show that these objects follow the $M_{\text{BH}} - \sigma_*$ relation.

5. DISCUSSION

5.1. Seyfert Type

We must examine the extent to which the results presented here are applicable to broad-line (Type 1) AGNs, since it is precisely in these objects that narrow emission-line widths are used to estimate σ_* . According to the unification hypothesis of Seyfert galaxies, the differences between Type 1 and Type 2 sources arise from orientation alone (e.g., Antonucci & Miller 1985), such that the BLR in Type 2 AGNs is hidden from direct view by an obscuring torus. In this picture, the NLR is an extended, roughly isotropic region extending far beyond the torus. Thus, our results should apply to both AGN types. On the other hand, it is possible that the fractional incidence of blue wings depends on the obscuring geometry, which in turn would depend on Seyfert type. This could result, for instance, if the torus is partially responsible for collimating the ionizing radiation field (see, e.g., Tadhunter & Tsvetanov 1989). That said, to first order at least, our results should apply to Type 1 and Type 2 objects. We offer two lines of evidence to support this.

First, if we consider well-studied, unbiased samples of Seyfert galaxies, such as that derived from the Palomar survey

⁷If d_x is the difference between the observed $[\text{OIII}]$ line width and the Tremaine et al. (2002) prediction based on the M_{BH} measurement, and d_y is the difference between the observed M_{BH} and that predicted by the measured $[\text{OIII}]$ line width, then $d_{\perp} = d_x d_y / \sqrt{d_x^2 + d_y^2}$. We (arbitrarily) define $d_{\perp} > 0$ if the point lies below the Tremaine et al. (2002) line. We choose this statistic because it does not assume an independent variable.

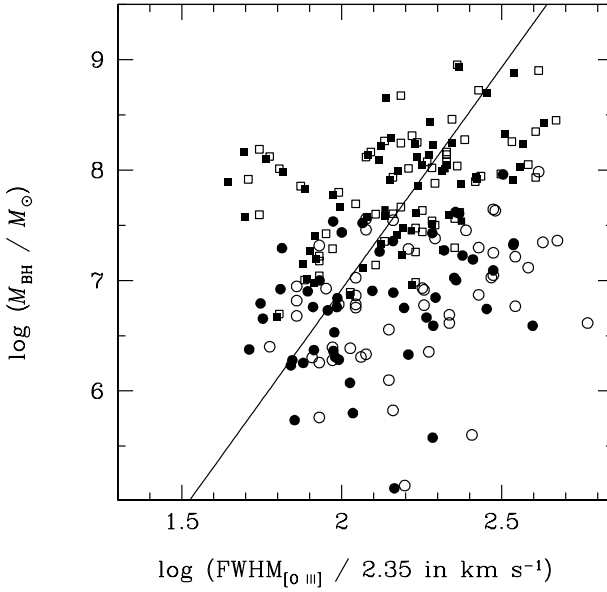


FIG. 4.— M_{BH} vs. [O III] line width for the Grupe & Mathur (2004) sample. We use the FWHM in this case because it is the quantity published. Open symbols are a reproduction of Figure 1 in Grupe & Mathur (2004), while filled symbols show the data for $\sigma_{[\text{OIII}]}$ corrected for the Eddington ratio according to Equation 3. Circles are NLS1s; boxes are broad-line Seyfert 1s. All measured quantities were taken from Grupe et al. (2004). The M_{BH} values come from the line width-luminosity-mass scaling relation of Kaspi et al. (2000). The solid line represents the $M_{\text{BH}} - \sigma_*$ relation from Tremaine et al. (2002).

(Ho et al. 1997a,b), we see that the distribution of bulge properties and nuclear emission-line widths are comparable for both Seyfert types. As shown in Table 1B of Ho et al. (2003), there is no statistical difference between the Type 1 and Type 2 objects in terms of Hubble type, absolute magnitude, and bulge luminosity, implying identical distributions of σ_* between the two groups. At the same time, the distribution of NLR line widths (see Table 2B of Ho et al. 2003) are also statistically equivalent. The similarities in both bulge and nuclear gas properties strongly suggest that Type 1 objects will show the same distribution in $\langle \sigma_g / \sigma_* \rangle$, as that seen here for Type 2 sources.

Second, we can directly test the hypothesis that $\langle \sigma_g / \sigma_* \rangle$ is invariant with respect to Seyfert type by using the study of Nelson & Whittle (1996), which provides σ_* and σ_g for 22 Type 1 and 44 Type 2 objects (these are the 66 objects with a tabulated [O III] line width and stellar velocity dispersion). Again, only FWHM measurements are available. We compare $\text{FWHM}_{[\text{OIII}]}$ with σ_* for these objects in Figure 5. The two samples largely appear to overlap. For Type 1 objects, $\langle \sigma_g / \sigma_* \rangle = 1.00 \pm 0.46$ while for Type 2 objects $\langle \sigma_g / \sigma_* \rangle = 1.22 \pm 0.78$. We use the K-S test to compare the distribution of σ_g / σ_* for each group and find that there is no statistically significant difference between the two; the probability of rejecting the null hypothesis that the two groups are drawn from the same parent population is $P_{\text{KS}} = 13\%$. When we remove the four obvious outliers, which are the powerful linear radio sources discussed by Whittle (1992b), the similarity between the two samples becomes even more apparent ($P_{\text{KS}} = 16\%$).

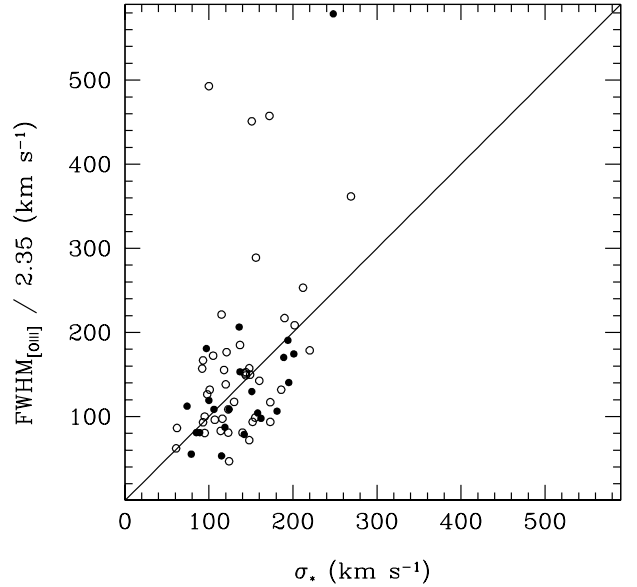


FIG. 5.— $\sigma_g = \text{FWHM}_{[\text{OIII}]} / 2.35$ plotted against σ_* for the Nelson & Whittle (1996) sample. Open symbols are Type 2 objects; filled symbols are Type 1 objects. The solid line denotes $\sigma_g = \sigma_*$. The extreme outliers are the powerful linear radio sources discussed by Whittle (1992b).

We can also ask whether $\Delta\sigma$ is correlated with Eddington ratio in Type 1 objects using the Nelson & Whittle (1996) sample. In Figure 3b we have overplotted the Type 1 objects from the Nelson & Whittle sample with measured σ_* , $L_{[\text{OIII}]}$, and $\text{FWHM}_{[\text{OIII}]}$. Seven of the velocity dispersions (NGC 3227, 3516, 4051, 4151, 4593, 5548, and Mrk 590) were updated from the more recent work of Nelson et al. (2004). We corrected the [O III] luminosity to our assumed cosmology. The correlation is not significant for the Type 1 objects ($\rho = 0.27$, $P_{\text{null}} = 0.21$), possibly because of the small number of objects considered, but they seem to trace roughly the trend defined by the Type 2 objects.

5.2. Aperture Effects

Because the SDSS aperture includes the central ~ 5 kpc of the galaxy a serious concern in the use of SDSS velocity dispersions is that rather than measuring the bulge velocity dispersion at a well-defined radius, a distance-dependent fraction of disk light may be included in the measurements. Both nuclear gas and stellar velocity dispersions may vary with radius. Therefore, we must examine the extent to which non-nuclear light contamination matters. Below we examine both the luminosity and kinematic distributions of stars and gas within the SDSS aperture to argue that our measurements are meaningful despite the large aperture. Rotational broadening is further discussed in the Appendix.

In the case of the gas, we expect the vast majority of the emission to come from the NLR at sub-kpc scales. After all, our sample was selected to show unambiguous AGN-like line ratios. Star-forming regions are the strongest contaminant,⁸ but if emission from star formation were important, then the spectra would look like those of H II regions or transition objects

⁸We note that of the three tracers considered here, [O II] is most susceptible to contamination by star formation. Only in low-metallicity H II regions, which are unlikely in the massive hosts of AGNs, is [O III] a major coolant, while [S II] is strong in H II regions only in the presence of shocks (e.g., Ho et al. 1997c; Kewley et al. 2001).

rather than bona fide AGNs. We can use the relation between NLR radius (R_{NLR}) and AGN luminosity to estimate the typical radius dominating the gas emission. Schmitt et al. (2003), using a sample of 60 Seyferts of both types imaged with the *Hubble Space Telescope*, find $\log R_{\text{NLR}} = (0.33 \pm 0.04) \times \log L_{\text{[OIII]}} - (10.78 \pm 1.80)$, with R_{NLR} in pc and $L_{\text{[OIII]}}$ in erg s^{-1} . The resulting range in physical size for our objects is $\sim 0.25 - 1.2$ kpc. At $z = 0.1$, the corresponding angular size ranges from $0.^{\prime\prime}14$ to $0.^{\prime\prime}67$, well within the SDSS aperture. Thus, we expect the radial variation in σ_g to be negligible.

We now turn to the luminosity distribution of starlight within the aperture. Unlike the gas, the stars are distributed throughout the aperture, and the velocity dispersion we measure may differ substantially from σ_* at R_e . We estimate the sizes of the bulges in our sample, and then infer the probable contamination to σ_* from disk light. For the median stellar velocity dispersion of $\sim 150 \text{ km s}^{-1}$ in our sample, the fundamental plane relation from Bernardi et al. (2003b) predicts $R_e \approx 4.5$ kpc. Alternatively, for a median galaxy mass of $\sim 5 \times 10^{10} M_\odot$, Kauffmann et al. (2003b) find a median $R_e \approx 3.3$ kpc. If the bulges are characterized by $R_e \approx 4$ kpc then the majority of the starlight in the ~ 5.4 kpc aperture originates in the bulge, and we are not probing stars much beyond an effective radius.

Even if the majority of starlight comes from the bulge, we still must consider the radial dependence of σ_* with radius. Jørgensen, Franx, & Kjægaard (1995) use 51 E/S0 galaxies available in the literature to derive an empirical aperture correction. For E/S0 galaxies, the integrated σ_* decreases outward as a function of radius, falling as a power law with slope -0.04 , relative to an aperture with a radius of $R_e/8$. On the other hand, Pizzella et al. (2004) find that the radial distribution in velocity dispersion is flat or slightly increasing outward in a sample of spiral (Sb-Sc) galaxies (see their Fig. 5). In early-type galaxies a large aperture will tend to underestimate σ_* for the bulge, while for late-type galaxies there may be a slight tendency in the opposite sense. Since our sample consists of early-type galaxies, on average the aperture variation most likely causes us to underestimate σ_* . Bernardi et al. (2003a) find a mean aperture correction of $\sim 7\%$ for a sample of early-type SDSS galaxies based on the empirical function from Jørgensen et al. (1995). In any case, the radial distribution of σ_* is quite flat. As a check, we can look for possible trends in $\langle \sigma_g / \sigma_* \rangle$ as a function of redshift. Since galaxy contamination, on average, should increase as a function of redshift, we might expect $\langle \sigma_g / \sigma_* \rangle$ to increase at higher redshift, if we assume $\sigma_g = \sigma_*$ intrinsically. We show $\langle \sigma_g / \sigma_* \rangle$ in three redshift bins ($z < 0.1$, $0.1 \leq z \leq 0.2$, and $z > 0.2$) in Table 1. We see no significant trend.

6. CONCLUDING REMARKS

Using a large sample of Type 2 AGNs selected from SDSS, we have systematically investigated the relation between stellar velocity dispersions (σ_*) and the kinematics of the emission-line gas (σ_g) as traced by optical forbidden lines ([O II] $\lambda 3727$, [O III] $\lambda 5007$, and [S II] $\lambda\lambda 6716, 6731$). We show that the widths of the low-ionization lines are gravitationally dominated, and may be used as a proxy for σ_* . We find that if the blue asymmetric wing of the [O III] line is removed, the width of the core component can also be used to estimate σ_* . The ionized gas in the central regions of active galaxies is evidently in approximate pressure support with the gravitational potential of the bulge stars of the host galaxy, consistent with the situation in inactive early-type galaxies (e.g., Bertola et al. 1995; Cinzano et al. 1999). The scatter in each of the σ_g - σ_* relations

is large, however, and we advocate their use only in statistical studies.

While not the primary goal of this study, our results offer some insights into the interaction between the AGN and the gas of the circumnuclear region. The nearly ubiquitous asymmetric blue wing of the [O III] line has long been recognized as indicative of radial motions in the NLR, presumably associated with an outflow. In this study, we have shown that this outflowing component is principally responsible for imparting supervirial motions to the gas. That lines with lower critical density generally lack this component suggests that it probably originates from a more compact region closer to the center. But what is the main physical driver of this component? We have shown that the most important variable appears to be the Eddington ratio. This finding may offer a useful outer boundary condition for constraining disk-wind models of the BLR (e.g., Murray & Chiang 1997; Proga, Stone, & Drew 1998; Proga, Stone, & Kallman 2000).

We thank an anonymous referee for comments that helped to clarify the manuscript. We are grateful for useful conversations with A. J. Barth, P. Martini, R. Narayan, A. Pizzella, and D. Proga. J. E. G. is funded by a National Science Foundation Graduate Research fellowship. L. C. H. acknowledges support by the Carnegie Institution of Washington and by NASA grants from the Space Telescope Science Institute (operated by AURA, Inc., under NASA contract NAS5-26555). We are grateful to L. Hao for making available her principal component analysis software, and to the entire SDSS collaboration for providing the extraordinary database and processing tools that made this work possible.

APPENDIX

ROTATIONAL BROADENING

Rotation must play a role in the nuclear kinematics. In particular, it is not unreasonable to expect some fraction of the nuclear gas to reside in a disk-like component. Whittle (1992b) concludes that rotation contributes at least partially to the [O III] line width in order to reproduce the observed relations between rotational velocity, inclination, and line width. Vega Beltrán et al. (2001) find that the ionized gas in a sample of 20 late-type disk galaxies is dominated by rotation. Without rotation velocities or inclination angles for our sample, it is difficult to directly examine the rotational contribution. Only the double-peaked emission lines provide evidence that rotation can dominate the kinematics, though they are only readily apparent in $\sim 1\%$ of the cases. However, we worry that rotational broadening may artificially increase our observed line widths. The same concern applies to the stellar velocity dispersions, since the SDSS aperture is sufficiently large that some disk light must contaminate the bulge σ_* .

We can estimate the contribution of rotational broadening to the observed scatter from both stellar and gaseous components by constructing a toy galaxy model with the average properties of our sample. In particular, we need a model for both the luminosity and radial velocity distributions in the disk. The rotational width is then simply

$$\sigma_{\text{rot}}^2 = \int (v - \bar{v})^2 I \, dv / \int I \, dv,$$

where I and v are both functions of radius, and \bar{v} is the luminosity-weighted mean velocity. For the intensity, we use an exponential distribution, $I = I_0 \exp(-R/R_d)$, with an exponential scale length of $R_d \approx 3$ kpc (Neistein et al. 1999). Since the gas emission is dominated by the NLR, the gas emission radii range from 0.25–1.2 kpc, while the stellar disk extends to a projected aperture radius of 2.7 kpc at $z = 0.1$.

The maximum circular rotational velocity, v_c , may be estimated using the Tully-Fisher relation. In order to account for the possible contamination of the host luminosity from the AGN, we use two different estimates of the absolute magnitude of the underlying host galaxy. The first uses the measured, K-corrected M_z values from Brinchmann et al. (2004a), corrected to our assumed cosmology. This yields an average $M_z = -21.98$ mag. One may worry, however, that AGN contamination is present even in Type 2 objects. We therefore indirectly estimate M_z in the following way. From the relation between concentration index and $(M/L)_z$ shown in Figure 13 of Kauffmann et al. (2003a) we can estimate the probable range in $(M/L)_z$. For our estimated mean concentration index of ~ 2.65 , we adopt a range in logarithmic mass-to-light ratios of $(M/L)_z = -0.1$ to 0.2 . If we assume that the typical host galaxy has a mass of $\sim 10^{10.7} M_\odot$, we find a range in absolute magnitude⁹ of $-21.74 < M_z < -22.49$. We are encouraged that the two methods are consistent. In what follows, we adopt $M_z = -22$ mag. Giovanelli et al. (1997) give the following form for the I -band Tully-Fisher relation: $M_I = -21 - 7.52x$, where $x = \log(v_c/2) - 2.5$. We estimate M_I using the color correction for S0 galaxies from Fukugita, Shimasaku, & Ichikawa (1995), $z - I_C = 0.21$ mag. Our resulting average v_c is 230 km s^{-1} . While we argue that our sample is dominated by early-type galaxies, we note that recent studies of the Tully-Fisher relation in S0 galaxies have found remarkably small offsets from the late-type population (Neistein et al. 1999; Hinz, Rieke, & Caldwell 2003).

As shown by Sofue et al. (1999), the rotation curves of active galaxies are comparable to those of quiescent galaxies, and so we use their measured rotation curves of barred and unbarred Sb and Sc galaxies as templates for our model. As a worst-case scenario, we only consider edge-on disks with $v_c = 230 \text{ km s}^{-1}$. The radius at which the rotation curve flattens is allowed to vary between 0.1 and 1 kpc, but the rising portion of the rotation curve need not be monotonic; in one of our models the velocity peaks at ~ 0.3 kpc, and then dips again before flattening at ~ 2.5 kpc. In the case of the gas, assuming emission radii between 0.25 and 1.2 kpc, σ_{rot} ranges from 8 to 74 km s^{-1} . The measured σ is simply the quadrature sum of the true σ_g and σ_{rot} , so a measured $\sigma_g \approx 150 \text{ km s}^{-1}$ may be overestimated by up to 15%. To estimate σ_{rot} in stars, we assume the same family of rotation curves but fix the emission radius at 2.7 kpc, for a maximum error of $\sim 12\%$ in σ_* . If we allow each component to independently assume its maximum error, and examine the case where $\sigma_g = \sigma_* = 150 \text{ km s}^{-1}$, we infer that the observed σ_g/σ_* may vary from 0.9 to 1.1. We therefore conclude that rotational broadening contributes to, but cannot fully account for, the observed scatter.

⁹To convert luminosity to absolute magnitude we assume, following Kauffmann et al. (2003a), that the z absolute magnitude of the Sun is $M_z \odot = 4.51$ mag at $z=0.1$.

REFERENCES

Abazajian, K., et al. 2004, AJ, 128, 502

Adams, T. F., & Weedman, D. W. 1975, ApJ, 199, 19

Akritas, M. G., & Siebert, J. 1996, MNRAS, 278, 919

Antonucci, R. R. J., & Miller, J. S. 1985, ApJ, 297, 621

Baldwin, J. A., Phillips, M. M., & Terlevich, R. 1981, PASP, 93, 5

Barth, A. J., Greene, J. E., & Ho, L. C. 2005, ApJ, 619, L151

Becker, R. H., White, R. L., & Helfand, D. J. 1995, ApJ, 450, 559

Bernardi, M., et al. 2003a, AJ, 125, 1817

—. 2003b, AJ, 125, 1866

Bertola, F., Cinzano, P., Corsini, E. M., Rix, H.-W., & Zeilinger, W. W. 1995, ApJ, 448, L13

Boroson, T. A. 2002, ApJ, 565, 78

Brinchmann, J., Charlot, S., Heckman, T. M., Kauffmann, G., Tremonti, C., & White, S. D. M. 2004a, (astro-ph/0406220)

Brinchmann, J., Charlot, S., White, S. D. M., Tremonti, C., Kauffmann, G., Heckman, T., & Brinkmann, J. 2004b, MNRAS, 351, 1151

Caldwell, N., Kirshner, R. P., & Richstone, D. O. 1986, ApJ, 305, 136

Cinzano, P., Rix, H.-W., Sarzi, M., Corsini, E. M., Zeilinger, W. W., & Bertola, F. 1999, MNRAS, 307, 433

Cinzano, P., & van der Marel, R. P. 1994, MNRAS, 270, 325

de Bruyn, A. G., & Wilson, A. S. 1978, A&A, 64, 433

De Robertis, M. M., & Osterbrock, D. E. 1984, ApJ, 286, 171

—. 1986, ApJ, 301, 98

Ferrarese, L., & Merritt, D. 2000, ApJ, 539, L9

Ferrarese, L., Pogge, R. W., Peterson, B. M., Merritt, D., Wandel, A., & Joseph, C. L. 2001, ApJ, 555, L79

Filippenko, A. V. 1985, ApJ, 289, 475

Filippenko, A. V., & Halpern, J. P. 1984, ApJ, 285, 458

Fillmore, J. A., Boroson, T. A., & Dressler, A. 1986, ApJ, 302, 208

Fisher, D. 1997, AJ, 113, 950

Fukugita, M., Ichikawa, T., Gunn, J. E., Doi, M., Shimasaku, K., & Schneider, D. P. 1996, AJ, 111, 1748

Fukugita, M., Shimasaku, K., & Ichikawa, T. 1995, PASP, 107, 945

Gebhardt, K., et al. 2000a, ApJ, 539, L13

—. 2000b, ApJ, 543, L5

Giovanelli, R., Haynes, M. P., Herter, T., Vogt, N. P., da Costa, L. N., Freudling, W., Salzer, J. J., & Wegner, G. 1997, AJ, 113, 53

Greene, J. E., & Ho, L. C. 2004, ApJ, 610, 722

Grupe, D., & Mathur, S. 2004, ApJ, 606, L41

Grupe, D., Wills, B. J., Leighly, K. M., & Meusinger, H. 2004, 127, 156

Gunn, J. E., et al. 1998, AJ, 116, 3040

Hao, L., et al. 2005, AJ, in press (astro-ph/0501059)

Heckman, T. M. 1980, A&A, 87, 152

Heckman, T. M., Kauffmann, G., Brinchmann, J., Charlot, S., Tremonti, C., & White, S. D. M. 2004, ApJ, 613, 109

Heckman, T. M., Miley, G. K., van Breugel, W. J. M., & Butcher, H. R. 1981, ApJ, 247, 403

Hinz, J. L., Rieke, G. H., & Caldwell, N. 2003, AJ, 126, 2622

Ho, L. C. 2004, in Carnegie Observatories Astrophysics Series, Vol. 1: Coevolution of Black Holes and Galaxies, ed. L. C. Ho (Cambridge: Cambridge Univ. Press), 293

Ho, L. C., Filippenko, A. V., & Sargent, W. L. W. 1993, ApJ, 417, 63

—. 1997a, ApJS, 112, 315

—. 1997b, ApJ, 487, 568

—. 1997c, ApJ, 487, 579

—. 2003, ApJ, 583, 159

Ho, L. C., & Peng, C. Y. 2001, ApJ, 555, 650

Ho, L. C., & Ulvestad, J. S. 2001, ApJS, 133, 77

Ivezic, Z., et al. 2002, AJ, 124, 2364

Jørgensen, I., Franx, M., & Kjærgaard, P. 1995, MNRAS, 276, 1341

Kaspi, S., Smith, P. S., Netzer, H., Maoz, D., Jannuzi, B. T., & Giveon, U. 2000, ApJ, 533, 631

Kauffmann, G., et al. 2003a, MNRAS, 341, 33

—. 2003b, MNRAS, 341, 54

—. 2003c, MNRAS, 346, 1055

Kauffmann, G., White, S. D. M., Heckman, T. M., Ménard, B., Brinchmann, J., Charlot, S., Tremonti, C., & Brinkmann, J. 2004, MNRAS, 353, 713

Kent, S. M. 1988, AJ, 96, 514

Kewley, L. J., Dopita, M. A., Sutherland, R. S., Heisler, C. A., & Trevena, J. 2001, ApJ, 556, 121

Kormendy, J., & Westpfahl, D. J. 1989, ApJ, 338, 752

Marconi, A., Risaliti, G., Gilli, R., Hunt, L. K., Maiolino, R., & Salvati, M. 2004, MNRAS, 351, 169

Mathur, S., Kuraszkiewicz, J., & Czerny, B. 2001, New Astronomy, 6, 321

McLure, R. J., & Dunlop, J. S. 2004, MNRAS, 352, 1390

Murray, N., & Chiang, J. 1997, ApJ, 474, 91

Neistein, E., Maoz, D., Rix, H.-W., & Tonry, J. L. 1999, AJ, 117, 2666

Nelson, C. H. 2000, ApJ, 544, L91

Nelson, C. H., Green, R. F., Bower, G., Gebhardt, K., & Weistrop, D. 2004, ApJ, 615, 652

Nelson, C. H., & Whittle, M. 1996, ApJ, 465, 96

Onken, C. A., Ferrarese, L., Merritt, D., Peterson, B. M., Pogge, R. W., Vestergaard, M., & Wandel, A. 2004, ApJ, 615, 645

Osterbrock, D. E. 1989, Astrophysics of Gaseous Nebulae and Active Galactic Nuclei (Mill Valley: University Science Books)

Pelat, D., Alloin, D., & Fosbury, R. A. E. 1981, MNRAS, 195, 787

Peterson, B. M., et al. 2004, ApJ, 613, 682

Pizzella, A., Corsini, E. M., Vega Beltrán, J. C., & Bertola, F. 2004, A&A, 424, 447

Pounds, K. A., Done, C., & Osborne, J. P. 1995, MNRAS, 277, L5

Proga, D., Stone, J. M., & Drew, J. E. 1998, MNRAS, 295, 595

Proga, D., Stone, J. M., & Kallman, T. R. 2000, ApJ, 543, 686

Rees, M. J., Phinney, E. S., Begelman, M. C., & Blandford, R. D., 1982, Nature, 295, 17

Schlegel, D. J., Finkbeiner, D. P., & Davis, M. 1998, ApJ, 500, 525

Schmitt, H. R., Donley, J. L., Antonucci, R. R. J., Hutchings, J. B., Kinney, A. L., & Pringle, J. E. 2003, ApJ, 597, 768

Sheth, R. K., et al. 2003, ApJ, 594, 225

Shields, G. A., Gebhardt, K., Salviander, S., Wills, B. J., Xie, B., Brotherton, M. S., Yuan, J., & Dietrich, M. 2003, ApJ, 583, 124

Shimasaku, K., et al. 2001, AJ, 122, 1238

Smith, E. P., Heckman, T. M., & Illingworth, G. D. 1990, ApJ, 356, 399

Smith, J. A., et al. 2002, AJ, 123, 2121

Sofue, Y., & Rubin, V. 2001, ARA&A, 39, 137

Sofue, Y., Tutui, Y., Honma, M., Tomita, A., Takamiya, T., Koda, J., & Takeda, Y. 1999, ApJ, 523, 136

Stoughton, C., et al. 2002, AJ, 123, 485

Strateva, I., et al. 2001, AJ, 122, 1861

Strauss, M. A., et al. 2002, AJ, 124, 1810

Tadhunter, C. N., & Tsvetanov, Z. 1989, Nature, 341, 422

Tremaine, S., et al. 2002, ApJ, 574, 740

Ulvestad, J. S., & Wilson, A. S. 1984, ApJ, 278, 544

Vega Beltrán, J. C., Pizzella, A., Corsini, E. M., Funes, J. G., Zeilinger, W. W., Beckman, J. E., & Bertola, F. 2001, A&A, 374, 394

Veilleux, S., & Osterbrock, D. E. 1987, ApJS, 63, 295

Wang, T., & Lu, Y. 2001, A&A, 377, 52

Whittle, M. 1985a, MNRAS, 213, 1

—. 1985b, MNRAS, 213, 33

—. 1992a, ApJ, 387, 109

—. 1992b, ApJ, 387, 121

Wilson, A. S., & Heckman, T. M. 1985, in Astrophysics of Active Galaxies and Quasi-Stellar Objects, ed. J. S. Miller (Mill Valley: University Science Books), 39

Wilson, A. S., & Willis, A. G. 1980, ApJ, 240, 429

Yee, H. K. C. 1980, ApJ, 241, 894

Yee, H. K. C., & Oke, J. B. 1978, ApJ, 226, 753

York, D. G., et al. 2000, AJ, 120, 1579

Yu, Q., & Tremaine, S. 2002, MNRAS, 335, 965

Zakamska, N., et al. 2003, AJ, 126, 2125